Manipulating single-photon emitter radiative lifetime in transition-metal dichalcogenides through Förster resonance energy transfer to graphene

R. Eddhib,[1] S. Ayari,[1] A. Hichri,[1] and S. Jaziri[1,2]

[1]*Faculté des Sciences de Bizerte Laboratoire de Physique des Matériaux Structure et Propriétés, Université de Carthage, 7021 Jarzouna, Tunisia*

[2]*Faculté des Sciences de Tunis Laboratoire de Physique de la Matière Condensée Département de Physique, Université Tunis el Manar, Campus Universitaire, 2092 Tunis, Tunisia*

(Received 11 May 2021; revised 31 August 2021; accepted 2 September 2021; published 21 September 2021)

Structural defects can crucially impact the optical response of monolayer (ML) thick materials as they are considered as efficient trapping sites for excitons. These trapped excitons are located below the free exciton emission. This phenomenon can give rise to a new type of emitters, known as "single-photon emitters" (SPEs). In this paper we outline the criteria, within our framework, by which single-photon emissions can be enabled in two-dimensional materials and we explore how these criteria can be fulfilled in atomically thin transition-metal dichalcogenides (TMD). In particular, we model the defects effect, in accordance with the most common experimental realisations, on the spatial autocorrelation function of the random disorder potential. Moreover, we provide a way to control the radiative lifetime of these emissions by a hybrid heterostructrue of a ML TMD with a graphene sheet separated by a dielectric material with a controlled thickness, which enables Förster resonance energy transfer process. Our paper predicts that the corresponding SPEs quenched radiative lifetime, which depends strongly on the dielectric environment, will be in the picosecond range. The range of our calculated exciton radiative lifetime in graphene-TMD heterostructure is consistent with that found in recent measurements.

DOI: 10.1103/PhysRevB.104.115426

I. INTRODUCTION

TMDs have become a hot spot for two-dimensional material investigations. In fact, atomically thin TMDs, which follow the common formula MX_2 (M = Mo, W and X = Se, S) have raised considerable attention in both physical science and material engineering due to their unique optical properties [1–5]. Indeed, owing to the large carrier effective masses, the two-dimensional spatial confinement and the reduced screening arising from the dielectric environment, the excitons in TMD benefit of a gigantic binding energies of about 200–500 meV. Hence, the excitonic states dominate the optical spectra even at room temperature [3,6–8]. Moreover, the truly two-dimensional nature of these materials offers a straightforward integration into existing photonic chip technology and this leads to a rich playground in manipulating their optoelectronic proprieties [3,6–9].

More recently, these monolayer (ML)-thick crystals have also emerged as promising materials for quantum information processing, where their optical response are characterised by the presence of a new type of SPE provided by the defects [2,10,11]. A single-photon emitter is one that produces a single photon in a single mode and that mode must be the same each time [2,10,11]. In this context, single-photon generation, which is an important building blocks for quantum technology has been achieved with a variety of systems in the past, most notably with, semiconductor quantum dots (QDs) [12], atomic defects such as nitrogen-vacancy centers in diamond [13], organic molecules [14], parametric down conversion [15], and more recently two-dimensional atomic crystals such as hBN [16–18]. Each system has its advantages, but also its limitations. In fact, the usability of single-photon sources critically depends on the stability of photon emission. It is, for example, still a challenge to find a single-photon source that is stable, can be replicated, and can be easily interfaced with electrical contacts, all desirable, if not essential, and features for efficient quantum communication devices [2,10,11]. For example, due to the large surface-to-volume ratio, colloidal semiconductor quantum dots with diameters of a few nanometers suffer from off times (blinking), spectral jumps (diffusion), and even disappearance of photon emission (photobleaching) [2,19–22]. However, the results on ML TMD are promising on various fronts. These materials are inorganic, stable and could be easily used to form an heterostructure with other two-dimensional materials, such as graphene [2,10,11].

In fact, many experimental groups such as Tonndorf *et al.* [2] have reported the observation of single-quantum emitters in atomically thin WSe_2. In their measurements they have not observed photo bleaching of the emitters for hours. Indeed, they prove that the same single center is still present after several days and cycling of the temperature between 10 and 300 K. This single-photon emission arises from the excitons trapped in local potential wells created by structural defects in the sample. The resulting localized excitons occur 50–120 meV below the free neutral exciton state in WSe_2 [2]. The defect in the TMD ML will introduces a confinement in all directions. In this case atomically thin semiconductor WSe_2 can be considered as a host for quantum dot-like defects [2,10,11].

These observations make evidence that TMDs can be emerged as a novel platform in which to realize stable single-photon emitter. This is the key future of the TMDs materials, combining thin structure with stable SPE source, where other systems such as InGaAs-QDs need to be buried about 100 nm away from any surface in order to escape noise from charge traps appearing there [23,24]. In the TMD ML case, this surrounding material is not only absent but can be designed purposefully by encapsulating the TMD by different materials. This proximity of TMD-QDs like to a surface allows potential for complete control over the emitter's surroundings. As proof of concept demonstration we are going to study the effect of coupling a TMD ML to a plasmonic structure (such as graphene [25]). The corresponding heterostructure requires nanometre-scale proximity to enable the Förster resonance energy transfer (FRET) mechanism [26–28]. This last process manifests in the transfer of a photoexcitation energy from a donor material (TMD) to an acceptor material (graphene) [29–31]. In other words, this effect is the conversion of an optical radiation emitted from a quantum device into so-called surface plasmon-polaritons on a weakly doped graphene [32–34]. We have chosen the weakly doped graphene as a quencher firstly because of its TMD matching structure and secondly because it is affordable and environmentally friendly [35,36]. Graphene derivatives like graphene oxide find extensive applications in biosensors and chemosensors because of their properties, in which they exhibit a remarkable quenching efficiency through FRET process up to 97% [37–43]. We highlight that in our theoretical work the quenching efficiency has reached 99% for very small separation distances.

We shall state that in our paper, we are not going to take into account variations in the trapping potential due to the atomic structure nor defect-induced changes in phonon characteristics. Our main focus lies on providing qualitative microscopic insights into the impact of localized bright exciton states on the optical responses of TMD ML. In this paper we are going to firstly state a dependence within our framework that is going to allow us to determine the conditions for which we obtain a SPE and prove its existing. Secondly, we are going to introduce the graphene induced quenching rate expression, which is applicable for all TMD materials. Thirdly, we are going to study the effect of a variety of spacers with ranging thickness on the SPE radiative lifetime of an exemplary TMD ML(WSe_2) with a weakly doped graphene sheet as a quencher material where we show the dependence of this radiative lifetime of the TMDs SPEs on this different spacer materials and its separation distance from the plasmonic material. Furthermore, we are going to highlight the effect of the random disorder parameters on the quenched radiative lifetime for an exemplary heterostructure (WSe_2/SiO_2/graphene). Finally, we are going to briefly determine the quenched radiative lifetime as a function of the interlayer distance for different ML TMD materials MX_2.

II. DEFECT AS A SPE SOURCE

The most trivial way to observe SPE is to ensure that, within a given detection spot size, only one quantum emitter exists. In this context, photoluminescence excitation spectroscopy reveals the excitonic nature of the emitters and provides evidence that these single excitons can be originate from free excitons trapped in local potential wells created by structural defects in the ML. In an experimental device these defects will be detuned and that this could generate single-photon emission even for large numbers of defects. Most commonly, defects in TMDs and other two-dimensional materials can be created by different mechanisms, like alpha-particle irradiation [44], residual impurities [45], atomic vacancy formation [46], strain from the substrate, high-temperature annealing, impurity doping [47] and chemical functionalization [45]. These localized sites are randomly distributed over each ML and it gives rise to a localization of excitons, which eventually causes stable and sharp emission lines, i.e., the single-photon emitters.

We model this structural imperfection (the inhomogeneous disorder that derived from defects), using a Gaussian random disorder potential that binds the center of mass of the electron-hole pair. This potential is created from a superposition of N random plane waves with random direction θ_i, random phase ϕ_i, V_0 the fluctuation amplitude, and finally L the correlation length:

$$V(\mathbf{R}) = \sqrt{\frac{2}{N}} V_0 \sum_{i=1}^{N} \cos\left(\frac{2\pi}{L} X \cos\theta_i + \frac{2\pi}{L} Y \sin\theta_i + \phi_i\right). \tag{1}$$

In the presence of defect, the momentum of the center-of-mass motion is no longer a good quantum number as in the case of free exciton. Such effect introduce an additional confinement in all directions similar to self-assembled ("natural") semiconductor QDs. However, the exciton in ML TMDs behaves as a massive particle subject to a disordered potential, leading to spatially localized eigenstates of the center-of-mass motion. To carry out the calculations of the energy and the wave function of localized exciton in disorder potential derived from defects, we need to resolve numerically the four-dimensional Wannier equations $H_X \Psi_X(\boldsymbol{\rho}, \boldsymbol{R}) = E_X \Psi_X(\boldsymbol{\rho}, \boldsymbol{R})$ (see Appendix A and Ref. [48] for more details about the localized exciton Hamiltonian H_X and the different approximations taken in our numerical calculation).

A. Effect of the correlation length on the localization-delocalization of energy states

Experimental and theoretical studies have proven that a disorder derived from defects can lead to a dramatic change in the physical behavior of the interband excitations, producing inhomogeneous spectral broadening and localization of all states, particularly in low-dimensional systems. In the same context, localization can also occur in time due to the fluctuations [42], even in the presence of interactions between particles, which is popularized in the recent publication with the term many-body localization [43]. We show in this part that for a random disorder potential and when its correlation length L is approximated to the average defect size, we have no localization of the exciton center-of-mass motion when the defect size is too small (in order of 1 nm), while for big defect

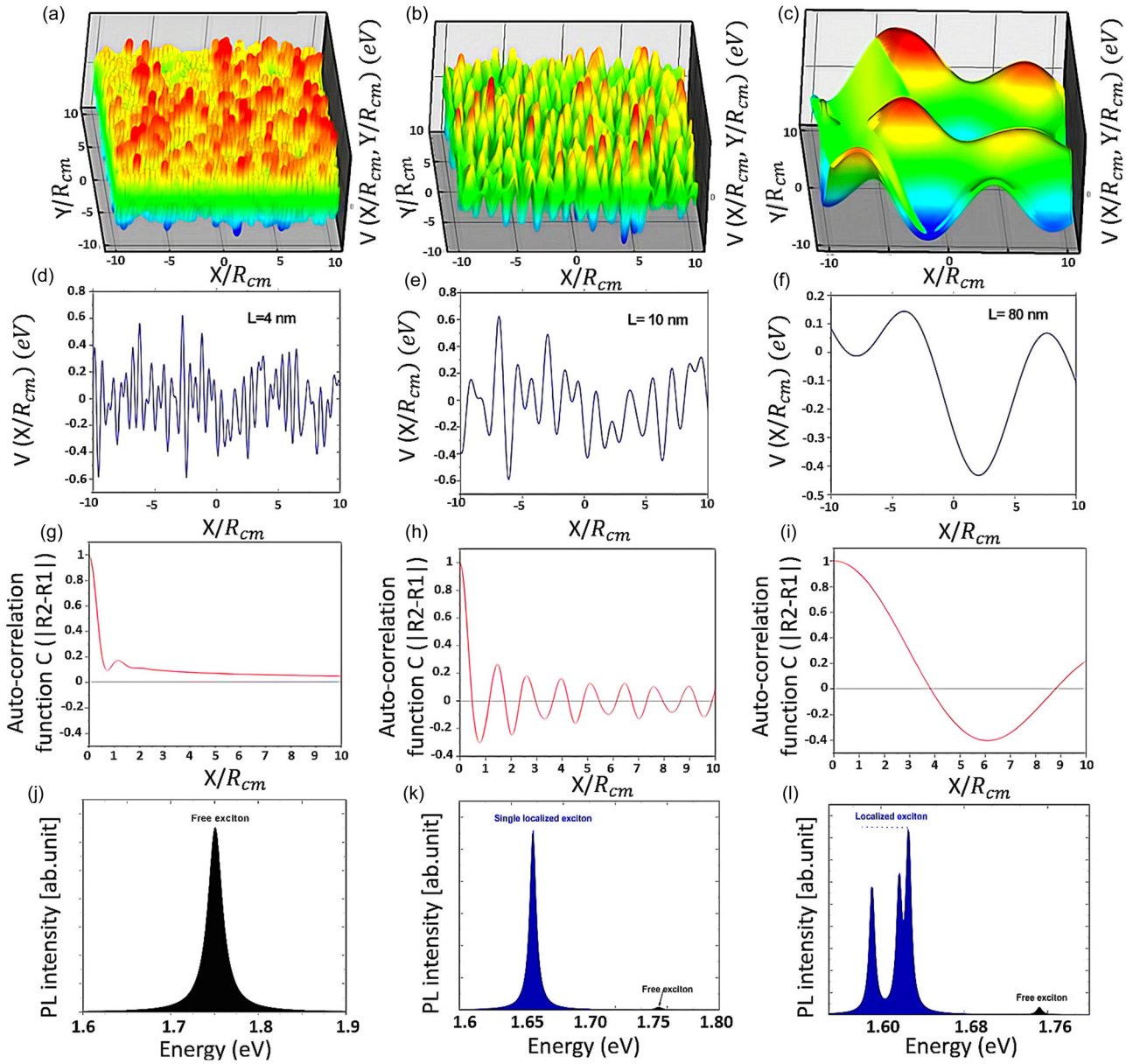

FIG. 1. [(a)–(c)] 3D-Schematic showing potential energy landscape due to defects under the influence of the correlation length, [(d)–(f)] a cut of the potential energy landscape for a fixed value of y. [(g)–(i)] The autocorrelation function C is shown as a function of $|R_2 - R_1|$ where we highlight its dependence on the correlation length. [(j)–(l)] PL spectrum's of defects in ML WSe_2 for (j) $L < R_{cm}$, (k) $L \approx R_{cm}$, and (l) $L > R_{cm}$ where we observe low-intensity PL peaks that are assigned to emissions from free excitons (pristine ML) and very intense peaks that are assigned to localized excitons we attribute this attenuation to the trapping of free exciton in the potential wells resulting in localized exciton. We note that the WSe_2 ML is deposited on the SiO_2/Si substrate and exposed to the air.

size (in order of 1 μm) the localization is maximized and it's impossible to obtain one SPE. It is important to note here, that we only obtain a SPE for an average defect size close to the center-of-mass localization length magnitude (≈10 nm).

In this section, in order to assure the localization of one single state we are going to further investigate our theoretical model given in Ref. [48] to determine the autocorrelation function $C(\boldsymbol{R_1}, \boldsymbol{R_2})$, which determines the so-called scale of roughness of the potential surface through the correlation length L and by that we confirm the conditions for which we have a SPE. The spatial autocorrelation function of the disorder potential $V(\mathbf{R})$ between two position vectors of the center of mass $\boldsymbol{R_1}$ and $\boldsymbol{R_2}$ can be written as [48]

$$C(\boldsymbol{R_1}, \boldsymbol{R_2}) = \frac{\overline{\langle V(\boldsymbol{R_1})V(\boldsymbol{R_2})\rangle} - \overline{\langle V(\boldsymbol{R_1})\rangle\langle V(\boldsymbol{R_2})\rangle}}{\overline{\langle V^2(\boldsymbol{R_1})\rangle}^{\frac{1}{2}}\overline{\langle V^2(\boldsymbol{R_2})\rangle}^{\frac{1}{2}}} = J_0\left(\frac{2\pi}{L}|\boldsymbol{R_1} - \boldsymbol{R_2}|\right), \quad (2)$$

here, $J_0(X)$ represents the Bessel function of the first kind order 0. The correlation function is quasi-periodic with respect

to the lag $|\boldsymbol{R_1} - \boldsymbol{R_2}|$ as soon as $|\boldsymbol{R_1} - \boldsymbol{R_2}| \geqslant L$, with a pseudo-period roughly equal to L. Notably, for $\boldsymbol{R} \in \mathbb{R}^2$ our disorder potential is characterized by zero-mean $\overline{\langle V(\mathbf{R})\rangle} = 0$ and constant standard deviation equal to $\sigma_V = \overline{\langle V^2(\mathbf{R})\rangle}^{\frac{1}{2}} = V_0$. It is worth noting that we can also define the autocovariance function, which is just the unnormalized correlation function $C_0(\boldsymbol{R_1}, \boldsymbol{R_2}) = \sigma_V^2.C(\boldsymbol{R_1}, \boldsymbol{R_2})$. Note that $C_0(\boldsymbol{R_1}, \boldsymbol{R_2})$ tend to σ_V^2 when $|\boldsymbol{R_1} - \boldsymbol{R_2}| \to 0$.

In the following we only address the property of the autocorrelation function, an important feature for this function is the decay shape, which represents the roughness degree of the random surfaces [for a truly random rough surface, $C(\boldsymbol{R_1}, \boldsymbol{R_2})$ usually decays to zero with the increase of $|\boldsymbol{R_1} - \boldsymbol{R_2}|$, where for a not really rough surface the autocorrelation function fluctuates around zero with the increase of $|\boldsymbol{R_1} - \boldsymbol{R_2}|$, and the larger the fluctuations are the less the roughness is] while the spatial decay rate depends on the distance over which two points on this potential surface become uncorrelated and this represents the correlation length L of an autocorrelation function [49].

In order to investigate the effect of the correlation length L on the roughness of the random surface and hence its effect on the localization of the exciton center-of-mass motion, we plot in Fig. 1 the disorder potential landscapes (3D and 1D) as well as the auto correlation function for three different value of L. We can clearly notice that the correlation length strongly affect the shape of the autocorrelation function as well as the potential roughness, which controls the localization/delocalization of the exciton states. In fact, the roughness of the potential surface decreases with the increasing of the correlation length L. Therefore, center-of-mass localization radius in the harmonic potential description $R_{cm} = \sqrt{\frac{\hbar}{M_X \omega_{cm}}}$ where ω_{cm} is the frequency of a 2D harmonic oscillator, three regimes can be distinguishable: (i) $L < R_{cm}$ [Fig. 1(a), 1(d), and 1(g)], this correspond to strong roughness of the potential surface and lead to unbound exciton center-of-mass states in a random potential, which can be explained by the expansion of its wave function over the heights of the potential lowering the role of potential fluctuation. This delocalized states regime is confirmed by the autocorrelation function where $C(\boldsymbol{R_1}, \boldsymbol{R_2})$ decreases monotonically from 1 to 0 with the increase $|\boldsymbol{R_1} - \boldsymbol{R_2}|$. (ii) $L > R_{cm}$, Figs. 1(c), 1(f), and 1(i)], this gives rise to a large potential width, which lead to strong disorder. In this case, the potential surface is smoother than the other regime [see Fig. 1(i)], and the exciton center-of-mass motion is strongly localized in the random disorder potential. In fact, in this regime since the localization length is very small compared to the correlation length, the confinement energy is large, so the quantification of the exciton center-of-mass motion into only one state is not likely to occur at these potential wells and we cannot obtain a SPE source in this regime. Hence, in order to assure the presence of a SPE we shall define the third regime (iii) where L is of the order of R_{cm} we obtain one single localized state in the disorder potential. We interpret this by the fact that defect size is approximated to the correlation length. Taken ML WSe_2 as an exemplary TMD, these results are clearly shown in Figs. 1(j)–1(l), in which we calculate the PL spectrum at T

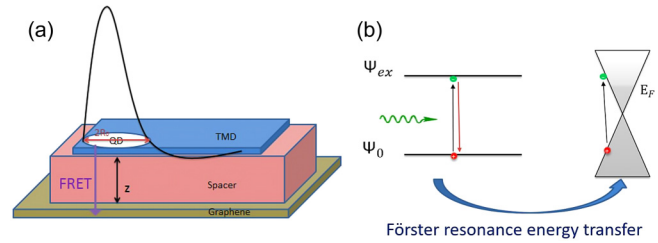

FIG. 2. (a) Schematic representation of the hybrid heterostructure of the FRET system, (b) the FRET mechanism from the TMD-QD like system to the graphene sheet.

$= 4$ K, using the following expression:

$$P^X \propto |\phi_{\vec{\Gamma}s}(\rho = 0)|^2 \left| \int \psi^{CM}_{n_x,n_y}(\boldsymbol{R})\, d^2\boldsymbol{R} \right|^2 \sigma(\hbar\omega - \hbar\omega_X),$$

where the Lorentzian $\sigma(\hbar\omega - \hbar\omega_X) = \frac{\sigma_X}{\pi[(\hbar\omega - \hbar\omega_X)^2 + \sigma_X^2]}$ express the energy conservation taking into account the state broadening. Here, ω_X is is the optical transition frequency with $E_X = \hbar\omega_X$, the phenomenological parameter σ_X is the half-width at half-maximum of the lines. $\psi^{CM}_{n_x,n_y}(R)$ is the center-of-mass wave function of localized exciton, $\phi_{\vec{\Gamma}s}(\rho)$ is the relative wave function of the exciton.

For $L > R_{cm}$, i.e., larger potential, the calculated spectra display several anharmonic peaks, which simulate in a realistic manner the low-energy peaks observed experimentally, while for $L \simeq R_{cm}$ and deep potential, we found a single localized state, which is also in an argument with the experience and the last one for $L < R_{cm}$ where the center-of-mass motion is free. In the follow we will concentrate our study on WSe_2 ML where $L = 100$ and $R_{cm} = 80$ in which we have a SPE that confirms what found in the experimental work [2]. After obtaining the SPE source we shall present the way to control this TMD-QD like system radiative lifetime by allowing the Förster resonance energy transfer process to occur when the ML TMD is coupled with the doped graphene sheet.

III. FRET: THEORETICAL APPROACH

In this part we are going to introduce the FRET quenching rate expression, which we have derived it from Velizhanin *et al.* [32] calculations in a way that fits our heterostructures. The procedure to make these FRET allowing structures consists of growing a dielectric spacer on top of a graphene sheet with a controllable thickness, then depositing a TMD ML on top of the dielectric spacer. The schematic hybrid system and FRET process are presented in Fig. 2.

The energy transfer from the TMD ML to the graphene sheet is based on the Coulomb interaction between the quasiparticle plasmon in graphene and the exciton of TMD-QD like system, corresponding to the Förster coupling. We define this interaction by the following expression:

$$H_{\text{int}} = \int d\mathbf{r} V_{\text{dip}}(\mathbf{r})(|\Psi_X\rangle\langle\Psi_0| + |\Psi_0\rangle\langle\Psi_X|)\hat{\rho}(\mathbf{r}), \quad (3)$$

where $\hat{\rho}(\mathbf{r}) = -e\chi(\mathbf{r})\chi^*(\mathbf{r})$ is the the charge density of graphene, with $\chi(\mathbf{r})$ and $\chi^*(\mathbf{r})$ are the created and destroyed

operators of an electron at position **r** within the graphene ML. The absolute value of the electron charge is denoted by $e = |e|$. $|\Psi_X\rangle$ and $|\Psi_0\rangle$ denote the localized exciton and the vacuum states respectively. The theoretical investigation of the FRET rate is done by evaluating the quenching rate that is expressed using the Fermi's golden rule and it results in [32]

$$\Gamma_q = -\frac{2}{(2\pi)^2\hbar}\int d\mathbf{q}|V_{\rm dip}(\mathbf{q})|^2 {\rm Im}[\Pi^{rpa}(\mathbf{q},\hbar\omega)]. \quad (4)$$

We have been using the polarization operator Π^{rpa} of the graphene that we have calculated with in the random phase approximation (RPA) because the polarization operator within the bare bubble approximation $\Pi_0(\mathbf{q},\hbar\omega)$ does not include the graphene's polarization self-consistently, which can become crucial at nonzero doping levels ($\mu > 0$), where the finite carrier density at the Fermi level leads to the efficient Coulomb screening within the graphene sheet [33]. Here μ is the chemical potential of the graphene sheet. So we evaluate the polarization operator within RPA as $\Pi^{rpa}(\mathbf{q},\hbar\omega) = \frac{\Pi_0(\mathbf{q},\hbar\omega)}{1-V(\mathbf{q})\Pi_0(\mathbf{q},\hbar\omega)}$ [34] where $V(\mathbf{q}) = 2\pi e^2/\tilde{k}q$ is the two-dimensional Fourier transform of the Coulomb potential within the graphene plane and $\tilde{k} = \frac{\varepsilon_{\rm spacer}+\varepsilon_{\rm vac}}{2}$ donates the effective dielectric constant encapsulating the graphene sheet. In this paper we are going to consider that $D < z$ where z is the interlayer distance (spacer thickness) between the TMD-QD like and the graphene, and D is the defect potential diameter. In Appendix B we detail the calculation of $V_{\rm dip}$ and it results [Eqs. (B12)] in the next expression of the quenching rate:

$$\Gamma_q = -\frac{2\pi e^2}{\hbar\,\varepsilon^2_{\rm spacer}}\left(2d_z^2 + d_\parallel^2\right)\int_0^\infty d\mathbf{q}\,\mathbf{q}{\rm Im}[\Pi^{rpa}(\mathbf{q},\hbar\omega)]e^{-2qz}, \quad (5)$$

where $d_\parallel$ and d_z are the projections of the ML TMD transition dipole **d** onto the graphene plane and the normal to this plane, respectively. We average these quantities over all the possible orientations with respect to the graphene plane, which yields in $\langle d_z\rangle$ and $\langle d_\parallel\rangle$. Here, $\langle d_z\rangle = e.a_0$ where a_0 is the thickness of TMD ML, or $\langle d_\parallel\rangle$ can be expressed as a function of optical dipole transitions by electromagnetic waves perpendicular to the layer, and its evaluated through elements of the optical matrix, which are related to the rate of spontaneous recombination of the exciton:

$$\langle d_\parallel\rangle^2 = \frac{e^2}{m_0^2\omega_X^2}|\phi_{\tilde{n}\tilde{l}}(\boldsymbol{\rho}=0)|^2\left|\int \psi^{CM}_{n_x,n_y}(\boldsymbol{R})d^2\boldsymbol{R}\right|^2 \times \left|\langle u_c|\boldsymbol{\epsilon}^\lambda_{\boldsymbol{q}}.\hat{\boldsymbol{p}}|u_v\rangle\right|^2, \quad (6)$$

here $\boldsymbol{\epsilon}^\lambda_{\boldsymbol{q}}$ is a unit vector characterizing the optical mode polarization λ, $\mathbf{q}$ is the photon wave vector and $\hat{\boldsymbol{p}}$ is the electron momentum operator. $\int \psi^{CM}_{n_x,n_y}(\boldsymbol{R})d^2\boldsymbol{R}$ represents the Fourier transform of the center-of-mass wave function taken at $\boldsymbol{K} = 0$. The momentum matrix element $\langle u_c|\boldsymbol{\epsilon}^\lambda_{\boldsymbol{q}}.\hat{\boldsymbol{p}}|u_v\rangle$ and the exciton wave function give rise to different selection rules. For the exciton center-of-mass wave function only the wave function with even n_x, n_y quantum number, giving a nonzero contribution in the calculation of the dipole moment. Also, $d_\parallel \neq 0$ only for $\tilde{1}s$ states in which the angular momentum $\mathrm{l} = 0$. The selection rules come also from $\langle u_c|\hat{\boldsymbol{p}}|u_v\rangle$, which depends on the nature of the Bloch functions. For bright exciton emission, the only nonzero elements of the valence-conduction coupling terms are $\langle u_c|\hat{p_\pm}|u_v\rangle$ for circularly polarized light $\sigma\pm$ propagating along the normal to the sample ($p_\pm = \frac{p_x \pm p_y}{\sqrt{2}}$), so that only optical modes with in-plane polarization components couple to these excitons. Therefore, using the $\boldsymbol{k.p}$ two-band model approximation, the momentum matrix element is given by

$$\langle u_c|\boldsymbol{\varepsilon}_\pm.\hat{\boldsymbol{p}_\pm}|u_v\rangle = \sqrt{\frac{m_0E_p}{2}}. \quad (7)$$

with $E_p = \frac{m_0E_g}{m_e}$ is the Kane energy for TMD materials obtained in the two band modes, E_g is the band-gap energy and m_e is the electron mass. Now, inserting the Eqs. (6) and (7) in the Eq. (5) the quenching rate can be rewritten as follows:

$$\begin{aligned}\Gamma_q &= -\frac{3\pi e^2c^3}{4n_0\omega_X^3\,\varepsilon^2_{\rm spacer}}\left(\frac{2(e.a_0)^2}{\langle d_\parallel\rangle^2}+1\right)\Gamma_{TMD} \\ &\quad\times\int_0^\infty d\boldsymbol{q}\,\boldsymbol{q}{\rm Im}[\Pi^{rpa}(\boldsymbol{q},\hbar\omega)]e^{-2qz} \\ &= \int_0^\infty d\boldsymbol{q}\,F(\boldsymbol{q},\hbar\omega), \end{aligned} \quad (8)$$

with Γ_{TMD} is the spontaneous emission rate of the localized exciton state j, which is given by

$$\begin{aligned}\Gamma_{TMD} &= \frac{4e^2}{3\hbar m_0c^3}n_0\omega_X E_p|\phi_{\tilde{n}\tilde{l}}(\rho=0)|^2\left|\int\psi^{CM}_{n_x,n_y}(\boldsymbol{R})d^2\boldsymbol{R}\right|^2 \\ &= \frac{8n_0\omega_X^3}{3\hbar c^3}\langle d_\parallel\rangle, \end{aligned} \quad (9)$$

here $n_0 = \sqrt{\tilde{k}}$ is the effective optical refraction index of the crystal environment. Using the above relations, we can now calculate the quenched radiative lifetime τ, which is given by $\tau^{-1}(z) = \Gamma_q + \Gamma_{TMD}$, we obtain

$$\tau^{-1}(z) = \Gamma_{TMD}\left[1 - \frac{3\pi e^2c^3}{4n_0\omega_X^3\,\varepsilon^2_{\rm spacer}}\left(\frac{2(e.a_0)^2}{\langle d_\parallel\rangle^2}+1\right) \times\int_0^\infty d\boldsymbol{q}\,\boldsymbol{q}Im[\Pi^{rpa}(\boldsymbol{q},\hbar\omega)]e^{-2qz}\right]. \quad (10)$$

We can also define the quenching efficiency as follows [41]:

$$\varphi_{\rm eff}(z) = \frac{\Gamma_q}{\Gamma_q+\Gamma_{TMD}} = \frac{\Gamma_q}{\tau^{-1}(z)}. \quad (11)$$

Our result coincides nicely with the result given in Ref. [33]. Note that we obtain a different expression compared to it since we are interested in the TMDs behavior and focused on its exciton's radiative decay rates. Using the last equations we gain the disired way to control the SPE radiative lifetime.

A. Investigation of the graphene effect on the TMDs SPEs

We exploit the derived equations to calculate the Förster induced quenching rate, efficiency and radiative lifetime of the SPE, for an exemplary TMD donor material, ML tungsten diselenide (WSe_2) in a hybrid heterostructure with a graphene sheet as a quencher material and SiO_2 as a spacer. We are going to adopt the data provided by the first part where we prove

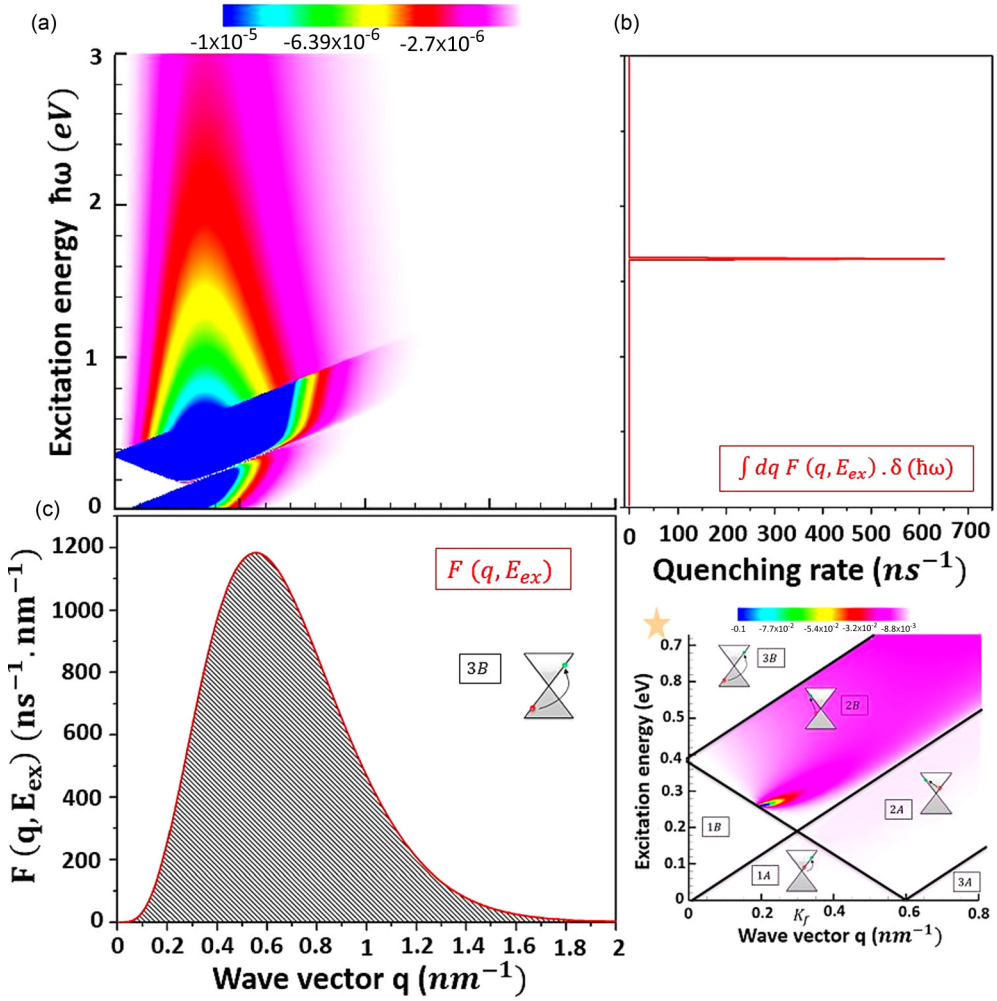

FIG. 3. (a) Plot of the $\mathrm{Im}[\Pi^{rpa}(q,\hbar\omega)]e^{-2qz}$ for a fixed distance between the TMD and the graphene layer (z = 5 nm). ($\star$) represents only the standard $\mathrm{Im}[\Pi^{rpa}(q,\hbar\omega)]$ plot, the white color emphasizes Region 1B ($q<\omega$, $q<2q_f-\omega/v_f$) of the phase space and it is protected from Landau damping arising from both interband and intraband transitions. The coloured regions are 1A ($\omega/v_f<q<2q_f-\omega/v_f$) and 2A ($\omega/v_f<q<2q_f+\omega/v_f$, $q>2q_f-\omega$), dominated by Landau damping resulting from intraband transitions, and 2B ($2q_f-\omega/v_f<q<\omega/v_f$, $\omega/v_f<2q_f+$q) and 3B ($q<\omega/v_f-2q_f$) dominated by indirect and direct interband transitions, respectively [33]. (b) represents the quenching rate of the SPE for an interlayer distance z = 5 nm and for a fixed excitation energy $E_X=1.654$ eV. (c) the red line represents the shape of the density-density imaginary part operator as a function of wave vector q and for the same fixed values where the hatched part represents the quenching rate as a function of the wave vector q.

that for a given L, V_0, R_{cm}, and N we have an SPE source with an energy of 1.654 eV and a decay rate of $\Gamma_{TMD}=0.625\,\mathrm{ns}^{-1}$. These disorder parameters will be the first key in enabling the FRET process. We begin our work by exploiting Eq. (8), where we show in Fig. 3(a), a plot of the imaginary part of the polarization operator of the weakly doped graphene layer multiplied by the distance quenching factor e^{-2qz} as a function of the excitation energy $\hbar\omega$ (eV) and the wave vector q (nm^{-1}) where we consider that the Fermi energy $E_F=0.2\,\mathrm{eV}$ and the Fermi velocity $v_f=10^{15}$ nm/s. We find rates of $\mathrm{Im}[\Pi^{rpa}(\boldsymbol{q},\hbar\omega)]e^{-2qz}$ ranging from $(-10^5\ \mathrm{eV}^{-1}\mathrm{nm}^{-2}$ to $0\,\mathrm{eV}^{-1}\mathrm{nm}^{-2})$ for z = 5 nm. We also show in Fig. 3(a) the electron-hole continuum or single-particle excitation regions in (q,E_X) space, which determines the absorption (Landau damping) of the external field at a given frequency and wave vector. In general the single-particle excitation continuum is defined by the nonzero value of the imaginary part of the polarizability function, $\mathrm{Im}[\Pi^{rpa}(\boldsymbol{q},\hbar\omega)]\neq 0$. In the graphene case both the intraband and the interband transition of the single-particle excitation are possible, and the boundaries are as showing in the inset of Fig. 3(a). In general, if the collective mode lies inside the single-particle excitation continuum then we expect the mode to be damped. For graphene, the plasmon lies inside the interband single-particle excitation continuum decaying into electron-hole pairs. Only in the region 1A of Fig. 3(a) that the plasmon is not damped, also the graphene plasmon does not enter into the intraband single-particle excitation and it exists for all wave vectors. The highest absorption rate is observed in the single-particle excitation interband regime (2B region), for the lowest excitation energy and for $q\to 0$ where the exponent e^{-2qz} in this term decays rapidly with q, which guarantees that when $\hbar\omega$ is fixed the dominant contribution to this term comes from lowest possible q where the imaginary part of the polarization operator is still nonzero.

TABLE I. The used spacer dielectric constant for determining the ML WSe_2 relative SPE energy E_X, radiative lifetime τ_{max} and its correspondent quenched radiative lifetime τ and quenching efficiency φ_{eff} for z = 6 nm and z = 10 nm.

Substrate	sapphire	Si_3N_4	h-BN	SiO_2	SiO_2	vacuum
ϵ_{spacer}	10	7	4.5	3.9	2.1	1
E_X(eV)	2.107	2.064	1.967	1.922	1.65	1.317
τ_{max}(ns)	179	100	15	12.8	1.6	0.24
$\tau(z = 6\,nm)$(ns)	1.37	1.05	0.72	0.63	0.27	0.04
$\varphi_{eff}(z = 10\,nm)\%$	88.5	84.3	50.6	50.6	19	19

We also mention that the optical absorption of the graphene layer decreases as a function of the increase of the interlayer distance. Now, to investigate the dependence of quenching rate Γ_q on the excitation energy we show in Fig. 3(b) the quenching rate for the adopted excitation energy of the WSe_2 QD like with a fixed interlayer distance (z = 5 nm) multiplied by the Dirac function $\delta(\hbar\omega - E_X)$, where we obtain a photoluminescence replica with an intensity corresponding to the quenching rate ($8.54\,ns^{-1}$) for that given distance and energy. In Fig. 3(c), we investigate the variation of the quenching rate as a function of the wave vector q where it represents a cut of the quenched polarizability of Fig. 3(a) for a fixed excitation energy $E_X = 1.654$ eV. We also find that the FRET quenching rate has a maximum at $q = 0.6\,nm^{-1}$ and its shape is governed by the $\mathrm{Im}[\Pi^{rpa}(\boldsymbol{q}, E_X)]$. This function is relative for two point charges located at the innermost portion of the graphene sheet. We state that for very small wave vectors, $\mathrm{Im}[\Pi^{rpa}(\boldsymbol{q}, E_X)] \approx 0$ (there is no screening inside the sheet) since very long wavelength perturbations correspond to charges being so far apart that they only experience the screening of the surrounding environment. For increasing wave vector $\boldsymbol{q}$, the charges get closer, so more of the field lines connecting them are confined to the interior of the graphene sheet.

We conclude that $\mathrm{Im}[\Pi^{rpa}(\boldsymbol{q}, E_X)]$ increases with **q** until it reaches near a maximum, and subsequently decreases with increasing $\boldsymbol{q}$ after the maximum due to the intrinsic inability of the medium to screen very short-wavelength excitations.

B. The environment effect on the SPEs quenched radiative lifetime

We investigate the effect of the spacer dielectric constant on the SPEs quenched radiative lifetime in a way to gain control over it. To get a first impression of this effect, we exploit Eq. (10) where the dielectric constant of the spacer (see Table I) interferes in the quenched radiative lifetime through the energy given by the QD-like WSe_2, its relative oscillator strength and finally through the screened excitations of the graphene translated by the RPA approximation. In Fig. 4, we evaluate all possible spacers materials, this will give us a control over the desired radiative lifetime where the dielectric constant is considered as a gate to tone the apparent radiative lifetime of the TMD material. This quenched radiative lifetime of the SPE is shown in Fig. 4(a) as a function of the spacer thickness for different dielectric constant, while in Fig. 4(c) we try to extrapolate the general behavior of this SPEs quenched radiative lifetime as a function of the dielectric constant taking into account the effect of ε_{spacer} on the RPA and for a spacer thickness z ranging from 0 nm to 40 nm. We find that this Förster induced radiative lifetime exhibits a smooth decay as a function of the spacer dielectric constant ranging from ($\tau_{max}^{sapphire} = 179$ ns; $\tau_{min}^{sapphire} = 3.26$ fs) relative to the lowest excitation energy, which corresponds to the highest spacer dielectric constant that of the sapphire spacer to ($\tau_{max}^{vacuum} = 0.24$ ns; $\tau_{min}^{vacuum} = 0.968$ fs) for the highest accessible excitation energy corresponding to the lowest spacer constant and that is of the vacuum. We show in Fig. 4(b) that changing the spacer material can push the limit of the quenching distance by 12 nm. We can mention that the lowest efficiency by distance curve is observed for the *vacuum*, and the biggest one is for the *sapphire*. We attribute this change to the direct effect of spacer dielectric constant on the SPEs energy and its corresponding radiative lifetime and also on the screening in the graphene sheet.

C. SPEs quenched radiative lifetime in the presence of different TMDs

We are going to shed light on the effect of the graphene sheet on other TMDs SPEs. Firstly, we should mention that the big difference between these materials in our framework

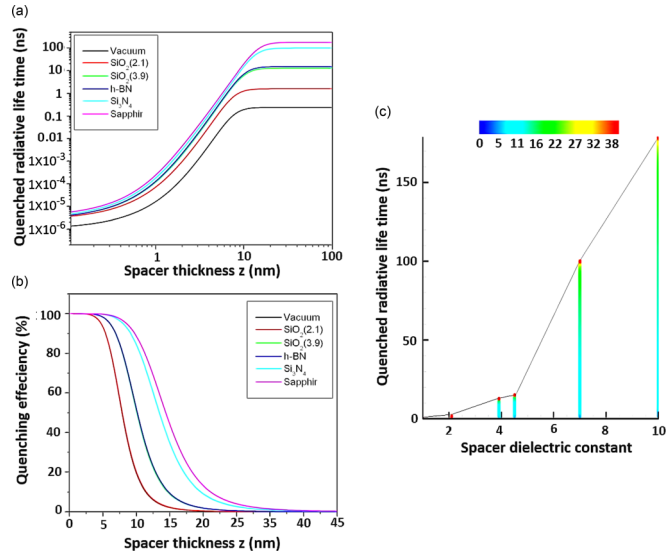

FIG. 4. (a) Numerical evaluation of quenched radiative lifetime of the TMD QD like system as a function of the interlayer distance (spacer thickness) and the spacer dielectric constant. (b) The FRET efficiency as a function of the interlayer distance and the spacer dielectric constant. (c) Extrapolation of the quenched radiative lifetime of the TMD QD-like system as a function of the spacer dielectric constant and the interlayer distance (color bar) ranging from 0 nm to 40 nm

TABLE II. Different ML TMD materials deposited on a SiO_2 substrate and their relative electron and hole effective masses $m_{e(h)}$, E_g gap energy, correspondent SPE energy E_X and radiative lifetime $\tau_{\max}$ we also provide the quenched radiative lifetime τ and the quenching efficiency φ_{eff} for a z = 5 nm spacer thickness.

TMD/SiO_2	WSe_2	WS_2	$MoSe_2$	MoS_2
$m_e(m_0)$ [50–53]	0.29	0.31	0.5	0.45
$m_h(m_0)$ [50–53]	0.36	0.42	0.6	0.54
E_g(eV) [54]	2.08	2.43	2.18	2.48
E_X(eV)	1.65	1.99	1.544	1.77
$\tau_{\max}$(ns)	1.6	0.7	0.12	0.19
$\tau(z = 6\,\text{nm})$(ps)	275	249	59	101
$\varphi_{\text{eff}}(z = 5\,\text{nm})(\%)$	83	83	74	71

consists mainly in the electron and hole effective masses, which are given in the Table II. Secondly, we show the difference in the SPEs radiative lifetime of TMD sheets (for a SiO_2 substrate) when the system is isolated from the graphene sheet, $\tau_{\max}^{WSe_2} - \tau_{\max}^{MoSe_2} = 1.41$ ns where the biggest radiative lifetime is attributed to ML WSe_2 $\tau_{\max}^{WSe_2} = 1.6$ ns or the lowest one is attribute for $MoSe_2$ $\tau_{\max}^{MoSe_2} = 0.15$ ps. In the presence of graphene and in close proximity the difference of the radiative lifetime becomes in order of $\tau_{\min}^{WSe_2} - \tau_{\min}^{MoSe_2} = 1.28$ fs where the lowest was attributed to the $MoSe_2$ with $\tau_{\min}^{MoSe_2} = 1.12$ fs and the highest was for the WSe_2 with $\tau_{\min}^{WSe_2} = 2.4$ fs. Changing the TMD material has proved, in the inset of Fig. 5(a), that it pushes the limit of the quenching distance by 4–6 nm and we can mention that the lowest efficiency by distance curve is observed for ML $MoSe_2$ while the biggest one is for the WSe_2 ML. The dominant variable here, which is considerably affecting the radiative lifetime, is the SPEs corresponding energies. To further investigate the effect of the excitation energy on the saturation regime defined as the radiative life time of the isolated source, we are going to compare the quenched radiative lifetime of three different energy regions. The first one is attributed to the TMD region of energy (1.3–2.3 eV), while the second is attributed to the low energy region (below 1.3 eV) and finally the third, which represents the high energy region (above 2.3 eV). We have plotted the quenched radiative lifetime of Fig. 5(b) as a function of the interlayer distance and the excitation energy, which is ranging from 0.5 eV to 4 eV, where we suppose that ($1/\Gamma_{TMD} = 1.6$ ns). Figure 5 shows that in the case of low excitation energies, the quenching of the radiative lifetime is mainly conducted by large spacer thicknesses but for small separation distances we have mainly the same effect (value). We observe also, that for high excitation energy the saturation regime is achieved within few nanometres (3–5nm). Compared to the TMD region, which have a smooth transition and make it possible to access any desirable quenched radiative lifetime easily from 0 nm to 20 nm.

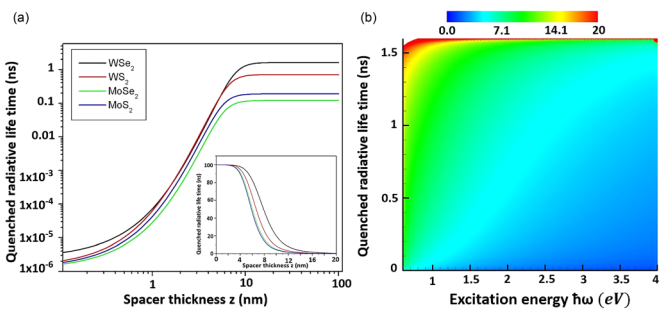

FIG. 5. (a) Numerical calculation of the the FRET radiative lifetime as a function of the interlayer distance for the different TMD materials on an SiO_2 substrate with an inset of their relative quenching efficiency. (b) The general behavior of the quenched radiative lifetime as a function of the excitation energy and the interlayer distance.

IV. CONCLUSION

In conclusion, we have discussed in the first part the localization of excitons in ML TMD due to a disordered structural potential, and the conditions for which each localization site can be viewed as a SPE. In the second part, we have showed that the localized exciton energy of this SPE can be transferred, via FRET to an adjacent 2D sheet of doped graphene. We have also proposed a method of manipulating single-photon emitter radiative lifetime in transition-metal dichalcogenides through FRET to graphene and we have analysed the fluorescence quenching efficiency in this TMD (SPE)-graphene complex. We predicted that the Förster quenching rate leads to a low radiative lifetime of this single-photon emission and we gained control over this quenching through two major gates, the dielectric spacer nature and the choice of the ML TMD material. Our paper predicts that the corresponding SPEs quenched radiative lifetime will be in the picoseconds range for a given distance, this time scale is in agreement with the recently measured exciton lifetime in these heterostructures [55–58].

ACKNOWLEDGMENTS

The authors gratefully acknowledge fruitful and stimulating discussions with Haithem Zahra.

APPENDIX A: LOCALIZED EXCITON STATES

To estimate the energies and the oscillator strength of the localized exciton, we use 2D effective-mass approximation. It is convenient to work in the center-of-mass frame and the physics of exciton is described by the following Schrödinger

equation:

$$\left[E_g - \frac{\hbar^2\nabla_{\boldsymbol{\rho}}^2}{2\mu} + V_{ky}(\boldsymbol{\rho}) - \frac{\hbar^2\nabla_{\boldsymbol{R}}^2}{2M_X} + V(\boldsymbol{R})\right]\Psi_X(\boldsymbol{\rho},\boldsymbol{R}) = E_X\Psi_X(\boldsymbol{\rho},\boldsymbol{R}), \tag{A1}$$

with $\boldsymbol{R} = \frac{m_e\boldsymbol{\rho_e}+m_h\boldsymbol{\rho_h}}{M_X}$, $\boldsymbol{\rho} = \boldsymbol{\rho_e} - \boldsymbol{\rho_h}$ are the position vector of the exciton center of mass and relative distance of the electron from the hole, respectively. Here $\boldsymbol{\rho_e}$ and $\boldsymbol{\rho_h}$ are the in-plane position vectors for the electron and the hole, respectively, E_g is the gap energy and $V(R)$ is the disorder potential derived from structural imperfections given by Eq. (1) in the main text. The electron-hole direct Coulomb interaction is treated here using the Rytova-Keldysh potential $V_{ky}(\rho)$ according to the widely accepted approach. $\mu = \frac{m_e m_h}{M_X}$ is the reduced effective mass, M_X is the exciton mass, m_e (m_h) is the electron (hole) effective mass given in terms of free electron effective mass units (m_0).

In our paper, it is assumed that the perturbation introduced by disorder is not sufficient to produce a transition from the exciton $1s$ state to higher states of the relative electron-hole motion. Hence, the exciton stays always in the $1s$ state and only its center-of-mass motion is affected by disorder. We make the following factorization ansatz for the localized exciton wave function solution of Eq. (A1):

$$\Psi_X(\boldsymbol{\rho},\boldsymbol{R}) = \phi_{\tilde{nl}}(\boldsymbol{\rho}) \times \psi^{CM}_{n_x,n_y}(\boldsymbol{R}), \tag{A2}$$

where $\phi_{\tilde{nl}}(\rho,\theta) = \sum_{n,|l|<n} C(n,l)\varphi_{n,l}(\boldsymbol{\rho})$ are the eigenvalue solutions of the relative Hamiltonian. $\phi_{\tilde{nl}}(\boldsymbol{\rho})$ expanded in terms of 2D-hydrogenic states $\varphi_{n,l}(\rho,\theta)$. $n = 1, 2, 3...$ is the principal quantum number, $l = 0, \pm1, \pm2, \pm3, ... \pm n-1$ is the angular momentum number and $\psi^{CM}_{n_x,n_y}(\boldsymbol{R}) = \sum_{n_x,n_y} D(n_x,n_y)$ $\frac{1}{\sqrt{n_x!n_y!}}\frac{1}{\sqrt{2^{n_x,n_y}}}\sqrt{\frac{1}{\pi R_{cm}^2}}\mathbf{H}_{n_x}(\frac{X}{R_{cm}})\mathbf{H}_{n_y}(\frac{Y}{R_{cm}})e^{-\frac{(X^2+Y^2)}{2R_{cm}^2}}$ is the center-of-mass wave function, obtained by the numerical diagonalization of the matrix resulting from the projection of the center-of-mass Hamiltonian on the basis of 2D harmonic oscillator. $R_{cm} = \sqrt{\frac{\hbar}{M_X\omega_{cm}}}$ is the center-of-mass localization radius in the harmonic potential description and ω_{cm} is the frequency of a 2D harmonic oscillator. $\mathbf{H}_{n_{x(y)}}$ are the Hermite polynomials. In this notation, the integers n_x, n_y are quantum numbers.

The solution of the Schrödinger equation for a localized exciton in a solid is

$$\zeta_X(\boldsymbol{R},\boldsymbol{\rho},z_e,z_h) = \Psi_X(\boldsymbol{\rho},\boldsymbol{R})u_{c,k}(\boldsymbol{r_e})u^*_{v,k}(\boldsymbol{r_h}),$$

where $u_{c,k}(\boldsymbol{r_e})$ and $u^*_{v,k}(\boldsymbol{r_h})$ are the Bloch functions taken at the points of high symmetry (K_τ, $\tau = \pm1$) of the valence (v) and conduction (c) bands. In our case, we neglect the possible mixtures with the other excitonic states. $\boldsymbol{r_{e(h)}} = (\boldsymbol{\rho_{e(h)}}, z_{e(h)})$ is the electron (hole) coordinates.

In order to calculate the optical matrix element obtained by considering the interaction with the first order electromagnetic field, it is convenient to introduce the Fourier transforms of the envelope-function $\phi_{n,l}(\rho,\theta)$ and $\psi^{CM}_{n_x,n_y}(\boldsymbol{R})$ defined in the plane of the 2D crystal:

$$\psi^{CM}_{n_x,n_y}(\boldsymbol{R}) = \frac{1}{(2\pi)^2}\iint e^{i\boldsymbol{K}.\boldsymbol{R}}\bar{\psi}^{CM}_{n_x,n_y}(\boldsymbol{K})d^2\boldsymbol{K}, \tag{A3}$$

$$\phi_{n,l}(\boldsymbol{\rho}) = \frac{1}{(2\pi)^2}\iint e^{i\boldsymbol{k}.\boldsymbol{\rho}}\bar{\phi}_{n,l}(\boldsymbol{k})d^2\boldsymbol{k}. \tag{A4}$$

We thus obtain the alternative expression

$$\zeta_X(\boldsymbol{R},\boldsymbol{\rho},z_e,z_h) = \frac{1}{(2\pi)^4}\iiint\int d^2\boldsymbol{K}d^2\boldsymbol{k}e^{i(\boldsymbol{K}.\boldsymbol{R}+\boldsymbol{k}.\boldsymbol{\rho})} \times \bar{\psi}^{CM}_{n_x,n_y}(\boldsymbol{K})\bar{\phi}_{n,l}(\boldsymbol{k})u_{c,k}(\boldsymbol{r_e})u^*_{v,k}(\boldsymbol{r_h}), \tag{A5}$$

with the center of mass $\boldsymbol{K}$ and relative $\boldsymbol{k}$ wave vectors are given, respectively by

$$\begin{cases}\boldsymbol{K} = \boldsymbol{k_e} + \boldsymbol{k_h}\\ \boldsymbol{k} = \frac{m_h\boldsymbol{k_e}-m_e\boldsymbol{k_h}}{M_X}.\end{cases} \tag{A6}$$

Using the following change of variables $(\boldsymbol{K},\boldsymbol{k}) \rightsquigarrow (\boldsymbol{k_e},\boldsymbol{k_h})$, with $d^2\boldsymbol{K}d^2\boldsymbol{k} = d^2\boldsymbol{k_e}d^2\boldsymbol{k_h}$, we can write

$$\zeta_X(\boldsymbol{R},\boldsymbol{\rho},z_e,z_h) = \frac{1}{(2\pi)^4}\iiint\int d^2\boldsymbol{k_e}d^2\boldsymbol{k_h}e^{i(\boldsymbol{k_e}.\boldsymbol{\rho_e}+\boldsymbol{k_h}.\boldsymbol{\rho_h})} \times \bar{\psi}^{CM}_{n_x,n_y}(\boldsymbol{K})\bar{\phi}_{n,l}(\boldsymbol{k})u_{c,k}(\boldsymbol{r_e})u^*_{v,k}(\boldsymbol{r_h}). \tag{A7}$$

We can then pass to discrete summations on the allowed states of the first Brillouin zone (BZ), because $|\boldsymbol{K}| \sim \frac{1}{L} \ll |\boldsymbol{b_1}|, |\boldsymbol{b_2}|$, $|\boldsymbol{k}| \sim \frac{1}{a_B} \ll |\boldsymbol{b_1}|, |\boldsymbol{b_2}|$ where $\boldsymbol{b_1}$ and $\boldsymbol{b_2}$ are the basis vectors of the reciprocal 2D lattice. Using the following approximation:

$$\sum_k (). \equiv \frac{S}{(2\pi)^2}\iint d^2k(),$$

the Eq. (A7) can be rewritten as

$$\zeta_X(\boldsymbol{R},\boldsymbol{\rho},z_e,z_h) = \frac{1}{S^2}\sum_{\boldsymbol{k_e}\in ZB}\sum_{\boldsymbol{k_h}\in ZB} e^{i(\boldsymbol{k_e}.\boldsymbol{\rho_e}+\boldsymbol{k_h}.\boldsymbol{\rho_h})} \times \bar{\psi}^{CM}_{n_x,n_y}(\boldsymbol{K})\bar{\phi}_{n,l}(\boldsymbol{k})u_{c,k}(\boldsymbol{r_e})u^*_{v,k}(\boldsymbol{r_h}). \tag{A8}$$

The Bloch functions $u_{c,k}(\boldsymbol{r_e})$ and $u^*_{v,k}(\boldsymbol{r_h}) = u_{h,-k}(\boldsymbol{r_h})$ vary slowly when $\boldsymbol{k_e}$ and $\boldsymbol{k_h}$ vary around the K point. We can write then

$$\zeta_X(\boldsymbol{R},\boldsymbol{\rho},z_e,z_h) = \frac{1}{S^2}\sum_{\boldsymbol{k_e}\in ZB}\sum_{\boldsymbol{k_h}\in ZB}\bar{\psi}^{CM}_{n_x,n_y}(\boldsymbol{K})\bar{\phi}_{n,l}(\boldsymbol{k})e^{i\boldsymbol{k_e}.\boldsymbol{\rho_e}} \times u_{c,k_e}(\boldsymbol{r_e})e^{i\boldsymbol{k_h}.\boldsymbol{\rho_h}}u^*_{v,k_h}(\boldsymbol{r_h}), \tag{A9}$$

$$\zeta_X(\boldsymbol{R},\boldsymbol{\rho},z_e,z_h) = \frac{1}{S}\sum_{\boldsymbol{k_e},\boldsymbol{k_h}\in ZB}\bar{\psi}^{CM}_{n_x,n_y}(\boldsymbol{K})\bar{\phi}_{n,l}(\boldsymbol{k})\Upsilon_{c,k_e}(\boldsymbol{r_e}) \times \Upsilon^*_{v,k_h}(\boldsymbol{r_h}), \tag{A10}$$

where

$$\Upsilon_{c,k_e}(\boldsymbol{r_e}) = \frac{1}{\sqrt{S}}e^{i\boldsymbol{k_e}.\boldsymbol{\rho_e}}u_{c,\boldsymbol{k_e}}(\boldsymbol{r_e}), \tag{A11}$$

$$\Upsilon_{v,k_h}(\boldsymbol{r_h}) = \frac{1}{\sqrt{S}}e^{i\boldsymbol{k_v}.\boldsymbol{\rho_h}}u_{v,\boldsymbol{k_h}}(\boldsymbol{r_h}), \tag{A12}$$

here $\boldsymbol{k_h} = -\boldsymbol{k_v}$. In fact, the hole state is related to the valence electron state by $\Upsilon_{k_h}(\boldsymbol{r}) = \hat{K}\Upsilon_{k_v}(\boldsymbol{r})$, with $\hat{K}$ being the time-reversal operator. In Fock representation, the electromagnetic field is written as

$$\hat{\boldsymbol{A}}_{\boldsymbol{q}}^{\lambda}(\boldsymbol{r},t) = \left(\frac{2\pi\hbar c}{n_0 qV}\right) \times \left[\boldsymbol{\epsilon}_{\boldsymbol{q}}^{\lambda} e^{i(\boldsymbol{q}.\boldsymbol{r}-\omega_q t)} a_{\boldsymbol{q},\lambda} + \boldsymbol{\epsilon}_{\boldsymbol{q}}^{\lambda} e^{-i(\boldsymbol{q}.\boldsymbol{r}-\omega_q t)} a_{\boldsymbol{q},\lambda}^{+}\right], \quad \text{(A13)}$$

$\boldsymbol{\epsilon}_{\boldsymbol{q}}^{\lambda}$ is a unit vector characterizing the optical mode polarization λ. The operator $a_{\boldsymbol{q},\lambda}^{+}$ ($a_{\boldsymbol{q},\lambda}$) creates (annihilates) a photon with wave vector $\boldsymbol{q}$ and polarization λ. The optical angular frequency is defined by $\omega_{\boldsymbol{q}} = \frac{c}{n_0}|\boldsymbol{q}|$, here n_0 is the effective optical refraction index of the crystal environment, c is the light velocity, and V is the normalized volume. The quantum mechanical interaction between radiation and matter is given by

$$\hat{H}_{\text{opt}}^{\lambda} = \frac{e}{2m_0 c}(\hat{\boldsymbol{A}}(\boldsymbol{r}).\hat{\boldsymbol{p}} + \hat{\boldsymbol{p}}.\hat{\boldsymbol{A}}(\boldsymbol{r})) + \frac{e^2}{m_0 c^2}\hat{\boldsymbol{A}}(\boldsymbol{r})^2. \quad \text{(A14)}$$

We treat the modification of the 2D system by the fields using the first order time-dependent perturbation theory, by ignoring the terms in $\hat{\boldsymbol{A}}^2$, in Eq. (A14), i.e., for sufficiently weak electromagnetic fields. In the Coulomb Gauge the terms $\boldsymbol{A}(\boldsymbol{r}).\hat{\boldsymbol{p}}$ and $\hat{\boldsymbol{p}}.\hat{\boldsymbol{A}}(\boldsymbol{r})$ coincide. So, in the Coulomb Gauge (div $\hat{\boldsymbol{A}} = 0$), the light-matter interaction Hamiltonian can be rewritten as

$$\hat{H}_{\text{opt}}^{\lambda} = \frac{e\hat{\boldsymbol{A}}(\boldsymbol{r})}{m_0 c}\hat{\boldsymbol{p}}, \quad \text{(A15)}$$

where $\hat{\boldsymbol{p}}$ is the electron momentum operator, e is the elementary charge. The light-matter coupling can be evaluated in the basis $\{|..., n_{\mathbf{q},\lambda}....\rangle \otimes |\zeta_X\rangle\}$. Here, $\{|..., n_{\mathbf{q},\lambda}....\rangle\}$ are the electromagnetic field states in Fock representation. The vector potential operator in the second quantization can be written as

$$\hat{\boldsymbol{A}}_{\boldsymbol{q}}^{\lambda}(\boldsymbol{r},t) = \hat{\boldsymbol{A}}_{\boldsymbol{q}}^{\lambda}(\boldsymbol{r})e^{-i\omega_q t} + \hat{\boldsymbol{A}}_{\boldsymbol{q}}^{+\lambda}(\boldsymbol{r})e^{i\omega_q t}. \quad \text{(A16)}$$

In our case, the initial state consists of an excitonic state without a photon $|i\rangle = |\zeta_X\rangle \otimes |0_{\mathbf{q},\lambda}\rangle$ while the final state consists of the crystal ground state $|\Psi_0\rangle$ with one photon $|f\rangle = |\Psi_0\rangle \otimes |1_{\mathbf{q},\lambda}\rangle$. The optical matrix element characterizing the transition from the 2D crystal ground state to the exciton state can be written as

$$M_{\boldsymbol{q},\lambda} = \left(\langle 1_{\mathbf{q},\lambda}| \otimes \langle\Psi_0|\right)\hat{\boldsymbol{A}}_{\boldsymbol{q}}^{\lambda}(\boldsymbol{r})\hat{\boldsymbol{p}}\left(|\zeta_X\rangle \otimes |0_{\mathbf{q},\lambda}\rangle\right). \quad \text{(A17)}$$

Hence, the optical matrix element can be rewritten as

$$M_{\boldsymbol{q},\lambda} = \sqrt{\left(\frac{2\pi\hbar c}{n_0 qV}\right)}\langle\Psi_0|e^{i\boldsymbol{q}.\boldsymbol{r}}\boldsymbol{\epsilon}_{\boldsymbol{q}}^{\lambda}\hat{\boldsymbol{p}}|\zeta_X\rangle. \quad \text{(A18)}$$

We define the oscillator strength of a transition by the dimensionless expression

$$f_{\epsilon_{\boldsymbol{q}}^{\lambda}} = \frac{2}{m_0\hbar\omega_0}|\bar{M}_{\boldsymbol{q},\lambda}|, \quad \text{(A19)}$$

where the optical transition frequency is $\omega_0 = |\omega_i - \omega_f|$. Here, $\omega_0 = \omega_X$, with $E_X = \hbar\omega_X$ and

$$\bar{M}_{\boldsymbol{q},\lambda} = \boldsymbol{\epsilon}_{\boldsymbol{q}}^{\lambda}\langle\Psi_0|e^{i\boldsymbol{q}.\boldsymbol{r}}\hat{\boldsymbol{p}}|\zeta_X\rangle, \quad \text{(A20)}$$

$$\bar{M}_{\boldsymbol{q},\lambda} = \frac{1}{S}\sum_{\boldsymbol{k_e},\boldsymbol{k_h}} \bar{\psi}_{n_x,n_y}^{CM}(\boldsymbol{K})\bar{\phi}_{n,l}(\boldsymbol{k})\left\langle\Upsilon_{c,k_e}\middle|\left\langle\Upsilon_{v,-k_h}^{*}\middle|e^{i\boldsymbol{q}.\boldsymbol{r}}\boldsymbol{\epsilon}_{\boldsymbol{q}}^{\lambda}.\hat{\boldsymbol{p}}\middle|\Psi_0\right\rangle$$

$$= \frac{1}{S}\sum_{\boldsymbol{k_e},\boldsymbol{k_h}} \bar{\psi}_{n_x,n_y}^{CM}(\boldsymbol{K})\bar{\phi}_{n,l}(\boldsymbol{k})\left\langle\Upsilon_{c,k_e}\middle|e^{i\boldsymbol{q}.\boldsymbol{r}}\boldsymbol{\epsilon}_{\boldsymbol{q}}^{\lambda}.\hat{\boldsymbol{p}}\middle|\Upsilon_{v,k_v}\right\rangle, \quad \text{(A21)}$$

since $\boldsymbol{k_e}, \boldsymbol{k_v} \in$ BZ, and $|\boldsymbol{q}| \ll |\boldsymbol{b_1}|, |\boldsymbol{b_2}|$

$$\left\langle\Upsilon_{c,k_e}\middle|e^{i\boldsymbol{q}.\boldsymbol{r}}\boldsymbol{\epsilon}_{\boldsymbol{q}}^{\lambda}\hat{\boldsymbol{p}}\middle|\Upsilon_{v,k_v}\right\rangle = \delta_{\boldsymbol{k_e},\boldsymbol{k_v}+\boldsymbol{q}}\left\langle u_{c,k_\tau}\middle|\boldsymbol{\epsilon}_{\boldsymbol{q}}^{\lambda}.\hat{\boldsymbol{p}}\middle|u_{v,k_\tau}\right\rangle,$$

hence

$$\bar{M}_{\boldsymbol{q},\lambda} = \frac{1}{S}\sum_{\boldsymbol{k_e},\boldsymbol{k_h}} \bar{\psi}_{n_x,n_y}^{CM}(\boldsymbol{K})\bar{\phi}_{n,l}(\boldsymbol{k})\left\langle u_{c,k_\tau}\middle|\boldsymbol{\epsilon}_{\boldsymbol{q}}^{\lambda}.\hat{\boldsymbol{p}}\middle|u_{v,k_\tau}\right\rangle\delta_{\boldsymbol{k_e},\boldsymbol{k_v}+\boldsymbol{q}}. \quad \text{(A22)}$$

In Eq. (A22), the Kronecker δ ensures the momentum conservation. The center of mass and relative wave vectors can be rewritten as

$$\boldsymbol{K} = \boldsymbol{k_e} + \boldsymbol{k_h} = \boldsymbol{k_e} - \boldsymbol{k_v} = \boldsymbol{q},$$

$$\boldsymbol{k}* = \frac{m_h\boldsymbol{k_e} - m_e\boldsymbol{k_h}}{M_X} = \boldsymbol{k_e} - \frac{m_e}{M_X}\boldsymbol{q},$$

or $|\boldsymbol{q}| \ll \frac{\pi}{L}$, on the scale of $|\boldsymbol{q}|$ $\bar{\psi}_{n_x,n_y}^{CM}(\boldsymbol{q})$ is slowly varying, therefore $\bar{\psi}_{n_x,n_y}^{CM}(\boldsymbol{q}) = \bar{\psi}_{n_x,n_y}^{CM}(0)$,

$$\bar{M}_{\boldsymbol{q},\lambda} = \frac{1}{S}\bar{\psi}_{n_x,n_y}^{CM}(\boldsymbol{K}=0)\sum_{\boldsymbol{k_e}}\bar{\phi}_{n,l}(\boldsymbol{k_e})\boldsymbol{\epsilon}_{\boldsymbol{q}}^{\lambda}\left\langle u_{c,k_\tau}\middle|\hat{\boldsymbol{p}}\middle|u_{v,k_\tau}\right\rangle \quad \text{(A23)}$$

or

$$\sum_{\boldsymbol{k_e}}\bar{\phi}_{n,l}(\boldsymbol{k_e}) = \frac{S}{(2\pi)^2}\iint d^2\boldsymbol{k_e}\bar{\phi}_{n,l}(\boldsymbol{k_e}) = S\phi_{n,l}(\rho=0)$$

and

$$\bar{\psi}_{n_x,n_y}^{CM}(\boldsymbol{K}=0) = \iint \psi_{n_x,n_y}^{CM}(\boldsymbol{R})d^2\boldsymbol{R}.$$

Finally, the optical matrix element $\bar{M}_{\boldsymbol{q},\lambda}$ can be written as

$$\bar{M}_{\boldsymbol{q},\lambda} = \left(\iint \psi_{n_x,n_y}^{CM}(\boldsymbol{R})d^2\boldsymbol{R}\right)\phi_{n,l}(\rho=0)\boldsymbol{\epsilon}_{\boldsymbol{q}}^{\lambda}\left\langle u_{c,k_\tau}\middle|\hat{\boldsymbol{p}}\middle|u_{v,k_\tau}\right\rangle, \quad \text{(A24)}$$

then we can rewrite the oscillator strength as

$$f_{\epsilon_{\boldsymbol{q}}^{\lambda}} = \frac{2}{m_0\hbar\omega_X}\left|\left(\iint \psi_{n_x,n_y}^{CM}(\boldsymbol{R})d^2\boldsymbol{R}\right)\right|^2|\phi_{n,l}(\rho=0)|^2 \times \left|\left\langle u_{c,k_\tau}\middle|\boldsymbol{\epsilon}_{\boldsymbol{q}}^{\lambda}.\hat{\boldsymbol{p}}\middle|u_{v,k_\tau}\right\rangle\right|^2. \quad \text{(A25)}$$

The oscillator strength can also be expressed in terms of the dipole matrix element as

$$f_{\epsilon_{\boldsymbol{q}}^{\lambda}} = \frac{2m_0\omega_j^X}{\hbar}\left|\langle\Psi_0|\boldsymbol{\epsilon}_{\boldsymbol{q}}^{\lambda}\hat{\boldsymbol{r}}|\zeta_X\rangle\right|^2. \quad \text{(A26)}$$

For circularly polarized light $\sigma_{\pm}$ propagating along the normal to the sample ($p_{\pm} = \frac{p_x \pm i p_y}{2}$), so that only optical modes with in-plane polarization components couple to these

excitons:

$$|d_\parallel|^2 = e^2\left|\langle\Psi_0|\boldsymbol{\epsilon}_{\boldsymbol{q}}^{\lambda}\hat{\boldsymbol{r}}|\Psi_X\rangle\right|^2 = \frac{e^2}{(m_0\omega_X)^2}\left|\left(\iint \psi^{CM}_{n_x,n_y}(\boldsymbol{R})d^2\boldsymbol{R}\right)\right|^2|\phi_{n,l}(\rho=0)|^2 \times \left|\left\langle u_{c,k_\tau}\left|\hat{\boldsymbol{p}}_{\pm}\right|u_{v,k_\tau}\right\rangle\right|^2. \quad \text{(A27)}$$

APPENDIX B: 2D-COULOMB FOURIER TRANSFORMATION

1. The Coulomb potential due to a point charge

First, we find the 2D Fourier transform of Coulomb potential, created in-plane, by a unit charge positioned at a distance z out of plane. Specific coordinates of the charge are $(x_0; y_0; z_0)$ and the plane is defined by z = 0. The real-space Coulomb potential of the unit charge is

$$V(\mathbf{r}) = \frac{Q}{\varepsilon_{\text{spacer}}\sqrt{z_0^2+(x-x_0)^2+(y-y_0)^2}}, \quad \text{(B1)}$$

where the in-plane vector $\boldsymbol{r}$ = (x; y; 0). Its 2D Fourier transform is

$$V(\mathbf{q}) = \frac{Q}{\varepsilon_{\text{spacer}}}\int d\boldsymbol{r}\frac{e^{-i(\mathbf{q}.\mathbf{r})}}{\sqrt{z_0^2+(x-x_0)^2+(y-y_0)^2}}. \quad \text{(B2)}$$

By substituting $x - x_0 \to$ x and $y - y_0 \to$ y we obtain

$$V(\mathbf{q}) = \frac{Qe^{-i(\mathbf{q}.\mathbf{r}_0)}}{\varepsilon_{\text{spacer}}}\int d\boldsymbol{r}\frac{e^{-i(\mathbf{q}.\mathbf{r})}}{\sqrt{z_0^2+x^2+y^2}}, \quad \text{(B3)}$$

where $\boldsymbol{r_0} = (x_0; y_0; 0)$. Rewriting the integral equivalently in polar coordinates produces

$$V(\mathbf{q}) = \frac{Q\,e^{-i(\mathbf{q}.\mathbf{r}_0)}}{\varepsilon_{\text{spacer}}}\int \boldsymbol{r}\,d\boldsymbol{r}\frac{1}{\sqrt{z_0^2+\mathbf{r}^2}}\int d\theta e^{-iqr\cos\theta}. \quad \text{(B4)}$$

The angular integral is evaluated (in Mathematica, or using integral tables by, for example, Gradshteyn and Ryzhik) to produce

$$\int_0^{2\pi} e^{-iqr\cos\theta}d\theta = 2\pi J_0(\boldsymbol{q}.\boldsymbol{r}), \quad \text{(B5)}$$

where $J_0(x)$ is the Bessel function of the first kind. This results in

$$V(\mathbf{q}) = \frac{2\pi\,Q}{\varepsilon_{\text{spacer}}}e^{-i(\mathbf{q}.\mathbf{r}_0)}\int \boldsymbol{r}\,d\boldsymbol{r}\frac{1}{\sqrt{z_0^2+\mathbf{r}^2}}J_0(\boldsymbol{q}.\boldsymbol{r}). \quad \text{(B6)}$$

This integral is also evaluated in Mathematica or using Gradshteyn & Ryzhik to produce

$$V(\mathbf{q}) = \frac{2\pi\,Q}{\varepsilon_{\text{spacer}}\,q}e^{-i(\mathbf{q}.\mathbf{r}_0)}e^{-qz_0}. \quad \text{(B7)}$$

2. The Coulomb potential due to a dipole

The simplest way to obtain an in-plane potential of a dipole, located out of the plane, is to use the result for point charge Eq. (7), and treat dipole as a collection of point charges. We substitute $z_0 \to z + \delta z_i$, and similarly for x_0 and y_0. Then, the total potential of collection of charge Q_i with coordinates (x $+\delta x_i$; y $+\ \delta y_i$; z $+\ \delta z_i$) is

$$V_{\text{dip}}(\mathbf{q}) = \frac{2\pi}{\varepsilon_{\text{spacer}}q}\sum_i Q_i e^{-q(z+\delta z_i)}e^{-iq_x(x+\delta x_i)}e^{-iq_y(y+\delta y_i)}, \quad \text{(B8)}$$

assuming δx_i, δy_i, and δz_i small and performing the Taylor expansion of exponents yields

$$V_{\text{dip}}(\mathbf{q}) = \frac{2\pi}{\varepsilon_{\text{spacer}}q}\left[\sum_i Q_i e^{-qz}e^{-iq_x x}e^{-iq_y y} + \sum_i Q_i(-q\delta z_i - iq_x\delta x_i - iq_y\delta y_i)e^{-qz}e^{-iqr}\right]. \quad \text{(B9)}$$

The first right-hand side term disappears once we assume that $\sum_i Q_i = 0$ as is always the case for dipoles. The expression, then becomes:

$$V_{\text{dip}}(\mathbf{q}) = \frac{2e\pi}{\varepsilon_{\text{spacer}}\,q}(-qd_z - iq_x d_x - iq_y d_y)e^{-qz}e^{-i\boldsymbol{q}.\boldsymbol{r}}, \quad \text{(B10)}$$

where d_α, α = x; y; z are components of the dipole vector. It straightforwardly transformed into

$$V_{\text{dip}}(\mathbf{q}) = \frac{2e\pi\,i}{\varepsilon_{\text{spacer}}}\left(-id_z - \frac{q_x d_x}{q} - \frac{q_y d_y}{q}\right)e^{-qz}e^{-i\boldsymbol{q}.\boldsymbol{r}}. \quad \text{(B11)}$$

Further, we rewrite the scalar product as $q_x d_x + q_y d_y = qd_\parallel \cos\theta$, where $d_\parallel = (d_x; d_y; 0)$ and θ is the angle between q and $d_\parallel$. The result is then:

$$V_{\text{dip}}(\mathbf{q}) = \frac{2e\pi\,i}{\varepsilon_{\text{spacer}}}(-id_z - d_\parallel\cos\theta)e^{-qz}e^{-i\mathbf{q}.\mathbf{r}}. \quad \text{(B12)}$$

This expression is very similar to Eq. (A7) in [32], except for some sign differences in the brackets, related to certain conventions of how the dipole is positioned with respect to the plane. The specific signs become irrelevant when calculating the rate of energy transfer, since the energy transfer will only depend on $|V(\mathbf{q})|^2$. Another way to think about it is that the sign of specific projects of a transition dipole must not matter when obtaining results for experimentally observed rate since, semiclassically, the transition dipole is the amplitude of an oscillating dipole.

[1] C. Janisch, Y. Wang, D. Ma, N. Mehta, A. L. Elías, N. Perea-Lopez, M. Terrones, V. Crespi, and Z. Liu, Sci. Rep. **4**, 5530 (2014).

[2] P. Tonndorf, R. Schmidt, R. Schneider, J. Kern, M. Buscema, G. A. Steele, A. Castellanos-Gomez, H. S. J. van der Zant, S. M. de Vasconcellos, and R. Bratschitsch, Optica **2**, 347 (2015).

[3] B. Zhu, X. Chen, and X. Cui, Sci. Rep. **5**, 9218 (2015).
[4] J. Huang, T. B. Hoang, and M. H. Mikkelsen, Sci. Rep. **6**, 22414 (2016).
[5] A. T. Hanbicki, G. Kioseoglou, M. Currie, C. Stephen Hellberg, K. M. McCreary, A. L. Friedman, and B. T. Jonker, Sci. Rep. **6**, 18885 (2016).
[6] A. R. Klots, A. K. M. Newaz, B. Wang, D. Prasai, H. Krzyzanowska, J. Lin, D. Caudel, N. J. Ghimire, J. Yan, B. L. Ivanov *et al.*, Sci. Rep. **4**, 6608 (2014).
[7] A. Chernikov, T. C. Berkelbach, H. M. Hill, A. Rigosi, Y. Li, O. B. Aslan, D. R. Reichman, M. S. Hybertsen, and T. F. Heinz, Phys. Rev. Lett. **113**, 076802 (2014).
[8] A. T. Hanbicki, M. Currie, G. Kioseogloub, A. L. Friedmana, and B. T. Jonker, Solid State Commun. **203**, 16 (2015).
[9] C. Poellmann, P. Steinleitner, U. Leierseder, P. Nagler, G. Plechinger, M. Porer, R. Bratschitsch, C. Schuller, T. Korn, and R. Huber, Nat. Mater. **14**, 889 (2015).
[10] J. J. P. Thompson, S. Brem, H. Fang, J. Frey, S. P. Dash, W. Wieczorek, and E. Malic, Phys. Rev. Mater. **4**, 084006 (2020).
[11] A. Srivastava, M. Sidler, A. V. Allain, D. S. Lembke, A. Kis, and A. Imamoglu, Nat. Nanotechnol. **10**, 491 (2015).
[12] P. Michler, A. Kiraz, C. Becher, W. Schoenfeld, P. Petro, L. Zhang, E. Hu, and A. Imamoglu, Science **290**, 2282 (2000).
[13] I. Aharonovich, S. Castelletto, D. A. Simpson, C. H. Su, A. D. Greentree, and S. Prawer, Rep. Prog. Phys. **74**, 076501 (2011).
[14] P. Farrera, G. Heinze, B. Albrecht, M. Ho, M. Chavez, C. Teo, N. Sangouard, and H. De Riedmatten, Nat. Commun. **7**, 13556 (2016).
[15] D. C. Burnham and D. L. Weinberg, Phys. Rev. Lett. **25**, 84 (1970).
[16] T. T. Tran, K. Bray, M. J. Ford, M. Toth, and I. Aharonovich, Nat. Nano. **11**, 37 (2016).
[17] N. Chejanovsky, M. Rezai, F. Paolucci, Y. Kim, T. Rendler, W. Rouabeh, F. Fvaro de Oliveira, P. Herlinger, A. Denisenko, S. Yang *et al.*, Nano Lett. **16**, 7037 (2016).
[18] G. Grosso, H. Moon, B. Lienhard, S. Ali, D. K. Efetov, M. M. Furchi, P. J. Herrero, M. J. Ford, I. Aharonovich, and D. Englund, Nat. Commun. **8**, 705 (2017).
[19] H. J. Kimble, Nature (London) **453**, 1023 (2008).
[20] A. Beveratos, R. Brouri, T. Gacoin, A. Villing, J. P. Poizat, and P. Grangier, Phys. Rev. Lett. **89**, 187901 (2002).
[21] E. Knill, R. La, and G. J. Milburn, Nature (London) **409**, 46 (2001).
[22] S. V. Polyakov and A. L. Migdall, J. Mod. Opt. **56**, 104 (2009).
[23] M. J. Stanley, C. Matthiesen, J. Hansom, C. Le Gall, C. H. H. Schulte, E. Clarke, and M. Atature, Phys. Rev. B **90**, 195305 (2014).
[24] R. Stockill, C. Le Gall, C. Matthiesen, L. Huthmacher, E. Clarke, M. Hugues, and M. Atature, Nat. Commun. **7**, 12745 (2016).
[25] A. K. Geim and K. S. Novoselov, The rise of graphene, in *Nanoscience and technology: A collection of reviews from nature journals* (World Scientific, 2010), pp. 1–11.
[26] R. S. Swathi and K. L. Sebastian, J. Chem. Phys. **129**, 054703 (2008).
[27] R. S. Swathi and K. L. Sebastian, J. Chem. Phys. **180**, 086101 (2009).
[28] R. S. Swathi and K. L. Sebastian, J. Chem. Sci. **121**, 777 (2009).
[29] M. Selig, E. Malic, K. J. Ahn, N. Koch, and A. Knorr, Phys. Rev. B **99**, 035420 (2019).
[30] H. Zahra, D. Elmaghroui, I. Fezai, and S. Jaziri, J. Appl. Phys. **120**, 205702 (2016).
[31] J. Qu, D. Jiang, L. Wang, K. Liu, X. Xu, C. Yao, and W. Sun, J. Mater. Sci. **54**, 8450 (2019).
[32] K. A. Velizhanin and A. Efimov, Phys. Rev. B **84**, 085401 (2011).
[33] E. H. Hwang and S. Das Sarma, Phys. Rev. B **75**, 205418 (2007).
[34] B. Wunsch, T. Stauber, F. Sols, and F. Guinea, New J. Phys. **8**, 318 (2006).
[35] X. Wu, F. Mu, Y. Wang, and H. Zhao, Molecules **23**, 2050 (2018).
[36] F. Tian, J. Lyu, J. Shi, and M. Yang, Biosens. Bioelectron. **89**, 123 (2017).
[37] M. Yi, S. Yang, Z. Peng, C. Liu, J. Li, W. Zhong, R. Yang, and W. Tan, Anal. Chem. **86**, 3548 (2014).
[38] E. M. Narvaez, B. P. Lopez, L. B. Pires, and A. Merkoci, Carbon **50**, 2987 (2012).
[39] X. Wu, Y. Xing, K. Zeng, K. Huber, and J. X. Zhao, Langmuir **34**, 603 (2018).
[40] P. Zheng and N. Wu, Chem. Asian J. **12**, 2343 (2017).
[41] I. L. Medintz and N. Hildebrandt (Editors), *FRET-Forster Resonance Energy Transfer: From Theory to Applications* (John Wiley, Hoboken, 2013).
[42] S. Fishman, D. R. Grempel, and R. E. Prange, Phys. Rev. Lett. **49**, 509 (1982).
[43] R. Brandenberger and W. Craig, Eur. Phys. J. C **72**, 1881 (2012).
[44] P. K. Chow, R. B. Jacobs-Gedrim, J. Gao, T. M. Lu, B. Yu, H. Terrones, and N. Koratkar, ACS Nano **9**, 1520 (2015)
[45] I. Pelant and J. Valenta, *Luminescence Spectroscopy of Semiconductors* (Oxford University Press, Oxford, 2012).
[46] Z. Lin, B. R. Carvalho, E. Kahn, R. Lv, R. Rao, H. Terrones, M. A. Pimenta, and M. Terrones, 2D Mater. **3**, 022002 (2016).
[47] S. Sasaki, Y. Kobayashi, Z. Liu, K. Suenaga, Y. Maniwa, Y. Miyauchi, and Y. Miyata, Appl. Phys. Express **9**, 071201 (2016).
[48] S. Ayari, A. Smiri, A. Hichri, S. Jaziri, and T. Amand, Phys. Rev. B **98**, 205430 (2018).
[49] R. Celotta and T. B. Lucatorto (Editors), *Experimental Methods in the Physical Sciences* (Academic Press, New York, 1999).
[50] D. Van Tuan, A. M. Jones, M. Yang, X. Xu, and H. Dery, Phys. Rev. Lett. **122**, 217401 (2019).
[51] M. Danovich, I. L. Aleiner, N. D. Drummond, and V. I. Fal'ko, IEEE J. Sel. Top. Quantum Electron. **23**, 168 (2017).
[52] T. Sohier, M. Calandra, and F. Mauri, Phys. Rev. B **94**, 085415 (2016).
[53] A. Kormányos, G. Burkard, M. Gmitra, J. Fabian, V. Zólyomi, N. D. Drummond, and V. Falko, 2D Mater. **2**, 022001 (2015)
[54] F. A. Rasmussen and K. S. Thygesen, J. Phys. Chem. C **119**, 13169 (2015).
[55] G. Froehlicher, E. Lorchat, and S. Berciaud, Phys. Rev. X **8**, 011007 (2018).
[56] J. He, N. Kumar, M. Z. Bellus, H. Y. Chiu, D. He, Y. Wang, and H. Zhao, Nat. Commun. **5**, 5622 (2014).
[57] H. M. Hill, A. F. Rigosi, A. Raja, A. Chernikov, C. Roquelet, and T. F. Heinz, Phys. Rev. B **96**, 205401 (2017).
[58] M. Trushin, Phys. Rev. B **97**, 195447 (2018).